International Journal of Hydrogen Energy 228 (2026) 154698

Contents lists available at ScienceDirect

International Journal of Hydrogen Energy

journal homepage: www.elsevier.com/locate/he

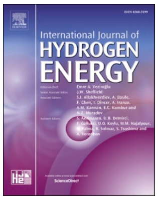

Iron-embedded hollow-out nitrogen-doped carbon nanoboxes catalyst with enhanced oxygen transport for improved ORR performance

Zheyan Tang [a], Hongwei Zhao [a,*], Lin Tao [a], Wenhao Liu [a], Lixiang Li [a,**], Yutong Shi [a], Jingang Zheng [a], Lin Wu [a], Han Zhang [a], Fang Di [a], Chengguo Sun [a,b], Zhihao Yao [c], Yanzhou Qin [d], Baigang An [a,***]

[a] *Key Laboratory of Energy Materials and Electrochemistry Research Liaoning Province, School of Chemical Engineering, University of Science and Technology Liaoning, 189 Qianshanzhong Road, Anshan, 114051, China*

[b] *School of Chemical Engineering, Nanjing University of Science and Technology, Nanjing, 210094, China*

[c] *High Temperature Materials Research Labs, School of Material Science and Engineering, University of Science and Technology Beijing, Beijing, 100083, China*

[d] *State Key Laboratory of Engines, Tianjin University, Tianjin, 300350, China*

ARTICLE INFO

Keywords:
Region-selective strategy
Fe-N_x and Fe nanoclusters
Hollow-out nitrogen-doped carbon nanoboxes
Oxygen transport
Oxygen reduction reaction

ABSTRACT

Constructing iron-nitrogen-carbon (Fe-*N*-C) catalysts with high intrinsic activity for the oxygen reduction reaction (ORR) remains challenging. Meanwhile, additional structural optimization is necessary to improve mass transport and attain higher power density for practical applications. Herein, using silicalite-1 zeolite as a template, we employed a region-selective strategy to construct iron-embedded hollow-out nitrogen-doped carbon nanoboxes (Fe-*N*-HOCNs) catalyst with coexisted Fe-N_x and Fe nanoclusters, and as an efficient ORR electrocatalyst for the zinc-air batteries (ZABs). Despite the Fe content of 4.73 wt% in Fe-*N*-HOCNs, it exhibits a high half-wave potential ($E_{1/2} = 0.87$ V), excellent mass activity (j_m, 658.17 mA mg^{-1}), and turnover frequency (TOF, 0.3808 e^- $site^{-1}$ s^{-1}), with ORR performance surpassing that of commercial Pt/C. This is attributed to the synergistic effect of coexisting Fe-N_x and Fe nanoclusters, which effectively lower the energy barrier of the ORR, optimizes the adsorption of reaction intermediates, and enhances electronic conductivity. Moreover, the abundant short-range, penetrable microporous/mesoporous channels overcome the diffusion limitations of O_2, significantly improving electrochemical wettability, accessibility, and utilization efficiency of the limited catalytic active sites, facilitating the exposure of active sites at the three-phase boundary. Finite element simulations reveal that the multidirectional hollow-out structure of Fe-*N*-HOCNs functions as interconnected pathways, substantially reducing O_2 transport resistance within the cathode catalyst layer. In ZABs, Fe-*N*-HOCNs enable the device to achieve a power density of 164 mW cm^{-2} and a specific capacity of 776 mA h g^{-1}, along with excellent rate performance.

1. Introduction

As a kind of electrochemical energy conversion device, fuel cells and metal-air batteries are strategically pivotal for future energy transition systems owing to their green operation, high efficiency, and operational stability [1,2]. In the core reaction systems of these devices, the oxygen reduction reaction (ORR) in the CCL, as a complex multiphase interface process involving four-electron transfer, has become a key bottleneck limiting the overall improvement of energy conversion efficiency due to its slow kinetics [3,4]. Currently, the approaches to increase the reaction rate of ORR mainly rely on Pt-based catalysts with excellent catalytic activity [5]. However, the scarcity and high preparation costs of Pt significantly restrict its large-scale application in energy devices. Therefore, the development of low-cost and high-performance non--precious metal ORR catalysts remains critically important but challenging.

Transition metal-nitrogen-carbon (*M*-*N*-C, M = Fe/Co/Ni) catalysts, featuring atomically dispersed metal-nitrogen group coordination

---

* Corresponding author
** Corresponding author
*** Corresponding author

E-mail addresses: hongwei0068@126.com (H. Zhao), lxli2005@126.com (L. Li), bgan@ustl.edu.cn (B. An).

https://doi.org/10.1016/j.ijhydene.2026.154698
Received 16 December 2025; Received in revised form 3 March 2026; Accepted 22 March 2026

centers, have emerged as a key research focus for the development of ORR electrocatalysts [6]. This can be attributed to their high atomic efficiency, tunable coordination microenvironments, exceptional intrinsic electrocatalytic activity, and the ability to control preparation costs [7]. Among these, Fe-*N*-C catalysts containing Fe-N_x active site are considered as one of the ideal candidate materials to replace Pt-based catalysts due to their extensive research foundation and promising application prospects [8]. In most Fe-*N*-C catalysts, the Fe-N_x active sites mainly exist in the form of Fe-N_4 and exhibit a nearly symmetrical planar configuration [9]. However, in the highly symmetric planar Fe-N_4 structure, the spatial charge distribution at the Fe center is constrained by symmetry and becomes uniform, lacking localized electron deficiency or enrichment, thereby diminishing its adsorption selectivity toward different oxygen-related intermediates (e.g., OOH*, O*, and OH*) [10,11]. Meanwhile, the d-p orbital hybridization between the Fe atom and N atom raises the d-band center of Fe and shifts it closer to the Fermi level. This electronic configuration strengthens the interaction between the high-energy Fe d orbitals and the antibonding orbitals of oxygen-related intermediates (e.g., the σ* orbital of *OH), thereby resulting in excessively high adsorption energies. Such strong adsorption not only leads to the accumulation of oxygen species on the catalyst surface but may also induce a shielding effect, ultimately suppressing the catalytic activity [12,13]. Additionally, during the prolonged ORR process, the Fe-N_4 active sites may experience detachment or degradation, which undermines the long-term stability of Fe-*N*-C catalysts [14].

Recent studies have demonstrated that while constructing Fe-N_x sites on carbon matrix with specific physicochemical properties, additional anchoring of metal nanoclusters or small nanoparticles can significantly improve the activity and stability of Fe-N_x catalysts [15]. For example, Wan et al. developed a Fe-*N*-C catalyst with a unique structure, featuring the coexistence of Fe nanoclusters and Fe-N_4 active sites on the surface of nitrogen-doped carbon quantum dots [16]. The efficient and unlocked electron transfer path exists between Fe nanoclusters and Fe-N_4, with an extremely short interaction distance, thereby forming a strong electronic coupling effect. The Fe nanoclusters optimize the adsorption strength of oxygen reduction intermediates on Fe-N_4 and also shorten the bond amplitude of Fe-N_4 with incoherent vibrations, ultimately enhancing the catalytic activity and durability of the Fe-N_4 sites by 60%. Similarly, Wang et al. synthesized a flexible multi-channel carbon fiber membrane incorporating coexisted Fe-N_4 sites and Fe nanoclusters [17]. The Fe nanoclusters induce substantial electron redistribution at the Fe-N_4 sites, enhancing the absorption capacity of *OOH during the rate-determining step at the Fe-N_4 site, and improving both the ORR activity and stability of the catalyst. Therefore, constructing a coexistence system of Fe-N_4 and Fe nanoclusters on appropriate carbon matrix represents an effective strategy to enhance the intrinsic ORR performance of Fe-*N*-C catalysts.

Furthermore, the ORR at the air cathode of battery involves a complex catalytic process at the solid-liquid-gas interface [18]. Effectively utilizing active sites located beyond the three-phase boundaries remains a significant challenge [19]. In traditional Fe-*N*-C catalysts, due to the complexities of high-temperature pyrolysis and heteroatom doping processes, a large number of Fe-N_x active centers are encapsulated within dense carbon layers, forming isolated sites. These isolated sites struggle to interact effectively with oxygen molecules, with only the Fe-N_x sites on the catalyst surface being able to participate in the reaction. For example, Kucernak et al. reported that only 4.5% of Fe-N_x sites functioned in their Fe-*N*-C catalysts [20]. Currently, the main approach is to increase the amount of catalyst used in the CCL. However, this inevitably increases the thickness of the CCL, and an excessively thick catalytic layer significantly hinders O_2 transport and electrolyte penetration, thereby adversely affecting the overall performance of the device [21]. Rather than simply increasing the number of active sites by thickening the CCL, a more effective strategy is to construct a highly accessible carbon matrix that simultaneously enables sufficient exposure of active sites and rapid transport of reactants and electrolytes within a limited thickness. For example, Ma et al. developed hierarchical porous nitrogen-doped carbon nanoboxes catalysts anchored with a high density of metal-N_x active sites via a polydopamine-assisted strategy [22]. The unique three-dimensional open pore structures markedly promote O_2 diffusion and electrolyte penetration, thereby accelerating ORR kinetics. Furthermore, by employing a Fe^{3+}-chelated polydopamine-assisted hollowing strategy, they also successfully constructed axially coordinated Fe-N_5 single-atom sites [23]. This coordination modulation enhances the intrinsic activity of sites, while synergizing with the open mass-transport channels to significantly improve overall device performance. Therefore, in the design and construction of Fe-*N*-C catalysts for ORR, it is not only necessary to optimize the activity of catalytic sites but also to regulate the morphology and microstructure of the carbon matrix to achieve abundant and stable multiphase interfaces, thereby satisfying the performance requirements of high-performance devices.

In this work, we employed a region-selective strategy to construct iron-embedded hollow-out nitrogen-doped carbon nanoboxes (Fe-*N*-HOCNs) with coexisted Fe-N_x and Fe nanoclusters, and as an efficient ORR electrocatalyst for the ZABs. Despite the Fe content of 4.73 wt% in Fe-*N*-HOCNs, it exhibits a high half-wave potential ($E_{1/2}$ = 0.87 V), excellent mass activity (j_m, 658.17 mA mg^{-1}), and turnover frequency (TOF, 0.3808 e^- $site^{-1}$ s^{-1}), with ORR performance surpassing that of commercial Pt/C. This is attributed to the coexistence of Fe-N_x and Fe nanoclusters, which effectively lowers the ORR energy barrier, optimizes intermediate adsorption, and enhances electronic conductivity. Additionally, the active sites are primarily concentrated within the porous framework of the Fe-*N*-HOCNs, and the abundant short-range, penetrable micro/mesoporous channels effectively overcome the limitations of O_2 diffusion, significantly improving the electrochemical wettability, accessibility, and utilization of the limited catalytic active sites in the micropores, thereby promoting the exposure of these sites at the three-phase boundaries both inside and outside of the Fe-*N*-HOCNs. More importantly, when Fe-*N*-HOCNs are assembled into ZABs, its multidirectional hollow-out structure serves as interconnected channels, effectively reducing the O_2 transport resistance within the CCL, the device power density can reach 164 mW cm^{-2}. This indicates that constructing the high-activity sites and abundant, stable multiphase interfaces within the carbon matrix of air cathodes can effectively enhance the performance of energy devices, thereby providing new opportunities for developing low-cost, earth-abundant catalysts.

2. Experimental section

2.1. Chemicals and regents

Tetraethyl orthosilicate (TEOS, 99%), Tetrapropylammonium hydroxide (TPAOH, 25 wt%), ammonia solution (NH_4OH, 25%), sulfuric acid (H_2SO_4, ≥96.0%), iron (II) phthalocyanine (FePc, 98%), Potassium hydroxide (KOH, ≥85.0%) are from Sinopharm Chemical Reagent Co. Ltd. Dopamine hydrochloride (DA, 98%), 1, 3, 5-trimethyl benzene (TMB, 98.0%) and ethanol (C_2H_5OH, ≥99.5%)are from Shanghai Aladdin Biochemical Technology Co., Ltd. Pluronic F127 and P123 are from Sigma-Aldrich. Hydrofluoric acid (HF, 48 wt%) is from Shanghai Macklin Biochemical Co., Ltd. The commercial 20% Pt/C catalyst is from TANAKA PRECIOUS METAL GROUP Co., Ltd. The commercial 75% RuO_2 catalyst is from Suzhou Sinero Technology Co., Ltd. Nitrogen (N_2, ≥99.999%), argon (Ar, ≥99.999%), and oxygen (O_2, ≥99.999%) were supplied by the Liaoning Guoyi New Material Technology Co., Ltd. All reagents were used without further purification. Deionized (DI) water was used in all experiments.

2.2. Synthesis of silicalite-1 (S-1) zeolite

Mix 12 mL of TPAOH (25 wt%) with 10 mL of DI water, then add 12 mL of TEOS. Stir the mixture continuously at 1400 rpm for 6 h. Transfer the resulting clear solution to a 200 mL polytetrafluoroethylene liner and place it in a stainless steel reactor. Place the autoclave in an oven and crystallize at 170 °C for 12 h. Centrifuge the solid sample, wash it several times with DI water and C_2H_6O, and dry it in an oven at 60 °C overnight. Finally, calcine the sample at 550 °C for 6 h. The obtained white powder is designated as silicalite-1 zeolite, referred to as S-1.

2.3. Synthesis of S-1@HO-mPDA and S-1@mPDA

Accurately weigh 0.2 g of P123 and 3.8 g of F127, and place them in a beaker. Add a mixture of 200 mL of DI water and 100 mL of C_2H_6O, and ultrasonically stir until P123 and F127 are completely dissolved. Then, add 0.6 g of S-1 to the solution and ultrasonically stir for 3 min to disperse. Next, add 6.0 g of DA, stir for 1 min, and then add 16 mL of TMB. Continue stirring until the solution becomes noticeably milky, then add 16 mL of NH_4OH. After reacting for 6 h, the product was centrifuged and vacuum dried at 80 °C to obtain the particles of hollow-out mesoporous polydopamine-coated S-1 zeolite (S-1@HO-mPDA) prepared based on the selective deposition strategy.

The synthesis process of mesoporous polydopamine-coated S-1 zeolite (S-1@mPDA) without hollow out structure is identical to that of S-1@OP-mPDA, except that F127 and P123 are not added.

2.4. Synthesis of Fe-N-HOCNs, Fe-N-CNs and Fe-NCs

Weigh 0.3 g S-1@OP-mPDA and add it to 30 mL of DI water, then ultrasonically stir for 2 min. Next, add 20 mL of a pre-prepared 0.005 M FePc solution, and stir in a water bath at 50 °C under vacuum for 8 h. Centrifuge and wash the product, then vacuum dry at 80 °C to obtain FePc/S-1@OP-mPDA particles. Using a horizontal tube furnace, heat the FePc/S-1@OP-mPDA from room temperature to 1000 °C at a rate of 5 °C min^{-1}. Maintain this temperature for 3 h under an Ar atmosphere, then allow it to cool naturally to room temperature. Wash the obtained sample with a mixture of 30 mL 40 wt% HF and 30 mL 0.01 M H_2SO_4, and finally freeze-dry the sample. The final sample, consisting of iron-embedded nitrogen-doped hollow out carbon nanoboxes, is referred to as Fe-*N*-HOCNs. Additionally, by adjusting the pyrolysis temperature to 900 and 1100 °C, the comparative samples Fe-*N*-HOCNs-900 and Fe-*N*-HOCNs-1100 were synthesized.

The synthesis process of the Fe-*N*-CNs sample without hollow-out structure with a fully dopamine-coated structure is identical to that of Fe-*N*-HOCNs, with the only difference being the use of S-1@mPDA.

In addition, we synthesized two other comparison samples. The synthesis steps are as follows:

The S-1@HO-mPDA was directly pyrolyzed at a high-temperature of 1000 °C to obtain the metal-free nitrogen-doped hollow-out carbon

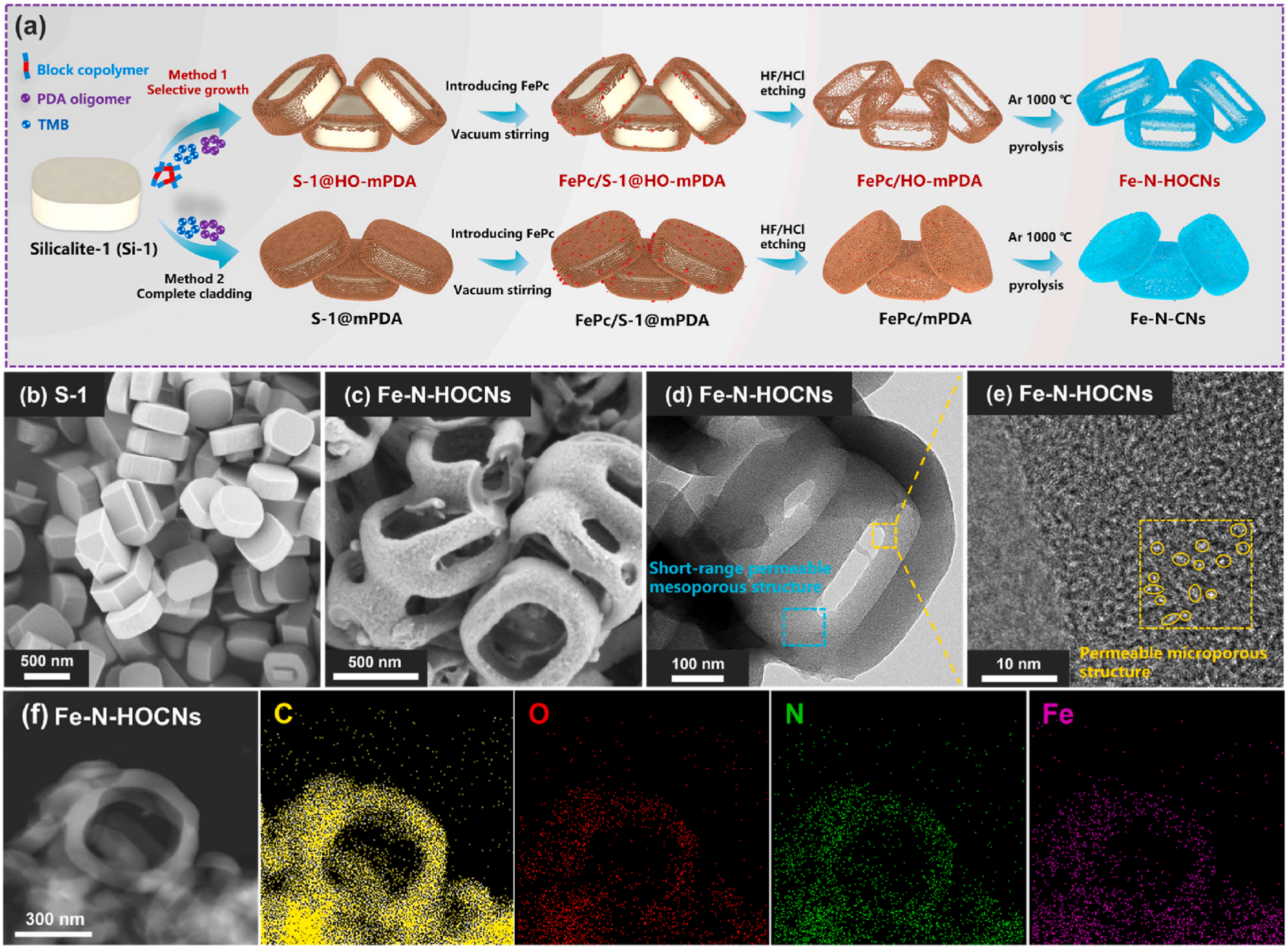

Fig. 1. (a) Schematic illustration for the synthesis of Fe-*N*-HOCNs and Fe-*N*-CNs samples. SEM images of (b) S-1, (c) Fe-*N*-HOCNs, (d-e) TEM and HRTEM images of Fe-*N*-HOCNs, (f) dark-field STEM image and EDS mappings of Fe-*N*-HOCNs. The bright white spot within the blue mark in (d) indicates a short-range penetrable mesoporous structure, and the bright white spot within the yellow mark in (e) represents a penetrable microporous structure. (For interpretation of the references to color in this figure legend, the reader is referred to the Web version of this article.)

nanoboxes, which was named HOCNs.

The FePc was directly pyrolyzed at a high-temperature of 1000 °C to obtain the Fe-N porous carbon sample, which was named Fe-NCs.

3. Results and discussion

3.1. Synthesis and characterization of catalysts

Fig. 1a shows the synthetic process of the iron-embedded hollow-out nitrogen-doped carbon nanoboxes (Fe-*N*-HOCNs) catalyst, while Fig. S2 displays the color changes of different samples at each step. First, the synthesized white silicalite-1 (S-1) zeolite was modified by using the block copolymers F127 and P123, followed by the introduction of polydopamine (PDA) and 1, 3, 5-trimethyl benzene (TMB). Due to the difference in packing densities of the block copolymers on various crystal faces of S-1, region-selective deposition of PDA was achieved. Additionally, the incorporation of TMB facilitated the creation of mesoporous structures within the deposited PDA layer [24]. Subsequently, the Fe-*N*-HOCNs catalyst (dark), featuring the hollow-out structure, was synthesized through a sequence of steps of vacuum impregnation with an iron-containing precursor (FePc), acid etching to remove the template and excess FePc, and high-temperature pyrolysis. The synthesis process of Fe-*N*-CNs without a hollow-out structure is similar to that of Fe-*N*-HOCNs, as no block polymer is added during the synthesis. The micromorphology of the samples was observed by scanning electron microscopy (SEM). As shown in Fig. 1b, S-1 exhibits a smooth surface and a nearly rectangular 3D structure. According to Fig. S3, S-1 displays three crystal directions: [100], [010], and [001], with the [010] and [100] planes being relatively flat, while the [001] plane exhibits some curvature [25]. In the S-1@OP-mPDA obtained after block polymer modification and PDA coating (Fig. S4), the framework-like mesoporous PDA selectively grows at the four intersecting edges between the [100] and [010] crystal planes of each S-1 crystal, as well as along the two curved surfaces in the [001] direction, thereby exposing two pairs of {100} and {010} crystal planes. It's worth noting that the dosage of TMB plays a pivotal role in regulating the mesoporous structure of the PDA layer. Owing to its robust hydrophobicity, TMB preferentially partitions into the hydrophobic cores of micelles self-assembled from block copolymers (P123/F127), effectively inducing pore expansion through a swelling effect. As shown in Fig. S5, a low TMB concentration (2 mL) results in insufficient swelling and restricted micelle expansion, confining the mesopore size of the PDA layer to 5~9 nm. Upon increasing the TMB volume to 8 mL, an optimal swelling effect is achieved, where the micelles reach an ideal size that facilitates the uniform deposition of PDA, yielding a well-distributed mesoporous structure with a moderate mesopore size (10~18 nm). However, an excessive TMB dosage (14 mL) leads to over-swelling or even structural instability of the micelles, causing a sharp increase in mesopore size to 19~25 nm. Simultaneously, the disruption of the emulsion equilibrium leads to uncontrolled morphology, shifting the process from interfacial deposition to bulk polymerization and eventually yielding a proliferation of PDA nanospheres. After vacuum impregnation of S-1@OP-mPDA with FePc, no additional substance formation was observed on the surface of FePc/S-1@OP-mPDA (Fig. S6). Following acid etching and pyrolysis, Fe-*N*-HOCNs (Fig. 1c) exhibited a significant hollow-out structure, originating from the exposed [100] and [010] crystal planes of S-1 in FePc/S-1@OP-mPDA. Meanwhile, most of the nano-framework remained stable, indicating the robustness and rigidity of the skeleton, and the obvious mesoporous structures can be observed in the nano-framework. However, only hollow-like structures were observed in the SEM images of Fe-*N*-CNs (Fig. S7), which was due to the non-selective deposition of PDA caused by the absence of block polymer modification during the synthesis process. Additionally, SEM images (Figs. S8 and S9) reveal that Fe-*N*-HOCNs synthesized at 900 °C and 1100 °C maintain morphologies roughly similar to that of the 1000 °C sample. Notably, pyrolysis at 900 °C leads to incomplete graphitization of the carbon layers, whereas increasing the temperature to 1100 °C induces excessive thermal contraction of the carbon framework, causing severe structural collapse and a markedly reduced carbon shell thickness.

The high-resolution transmission electron microscopy (HRTEM) image in Fig. 1d reveals the microstructure of the Fe-*N*-HOCNs. Fe-*N*-HOCNs possess a hollow-out quasi-cubic nano-framework structure, with short-range penetrable mesoporous structures embedded within the framework. Additionally, numerous penetrable micropores can also be observed in the carbon layer structure of the framework via HRTEM (Fig. 1e). The unique porous structures of Fe-*N*-HOCNs offer potential advantages as follows. As illustrated in the schematic (Fig. S10), the hollow-out structure can ensure that both the internal and external surfaces are fully exposed to the reaction environment, and the short-range mesopores can help to alleviate diffusion limitations, while the penetrable micropores are expected to increase the probability of interaction between limited active sites and O_2. In addition, a small amount of large-sized Fe nanoclusters is observed within Fe-*N*-HOCNs (Fig. S11a). The HRTEM analysis indicates that the lattice distance of Fe nanoclusters is approximately 0.23 nm [26], attributed to the Fe (110) crystal plane (Fig. S11b–c). Spherical aberration-corrected transmission electron microscopy reveals abundant Fe single-atoms and numerous small-sized Fe nanoclusters in Fe-*N*-HOCNs (Fig. S12), providing evidence for the coexistence of Fe-N_x and Fe nanoclusters Meanwhile, elemental mapping images (Fig. 1f) confirmed the homogeneous distribution of C, O, N, and Fe atoms in the Fe-*N*-HOCNs.

The powder X-ray diffraction (XRD) measurements were conducted to investigate the composition and structure of samples (Fig. 2a). A prominent diffraction peak centered at approximately 26.0° attributing to the graphite {002} plane was observed from all samples, indicating that PDA can be converted into graphitic carbon following high-temperature pyrolysis. However, in contrast to the hollow nitrogen-doped carbon nanoboxes (HOCNs) without FePc, the Fe-NCs, Fe-*N*-CNs and Fe-*N*-HOCNs all exhibited two distinct new phases of $FeN_{0.0324}$ phase (JCPDS No. 75-2127) and Fe phase (JCPDS No. 65-4899) [27–29]. The Fe-NCs were prepared via direct pyrolysis of FePc. The diffraction peaks observed at 43.5°, 50.7°, and 74.6° match the [111], [200], and [220] lattice planes of cubic $FeN_{0.0324}$, respectively. The weak diffraction peaks located at 44.6°, 65.0°, and 82.3° correspond to the [110], [200], and [211] planes of Fe phase. The formation of a small amount of Fe phases is primarily attributed to the slight aggregation of the FePc precursor during the introduction stage. During pyrolysis, some Fe atoms migrate and agglomerate into a small number of large-sized Fe nanoclusters, which is consistent with the results observed in HRTEM. Notably, the presence of the non-stoichiometric compound $FeN_{0.0324}$ (Fe-N_x) and Fe nanoclusters indicates that the pyrolysis process can modify the coordination environment of Fe atoms in FePc, leading to a change in the bonding configuration between Fe and N atoms and the formation of Fe nanoclusters. The synergistic effect between Fe-N_x sites and Fe nanoclusters could affect the adsorption capacity of the active site for oxygen containing species. Furthermore, comparative XRD pattern of Fe-*N*-HOCNs samples pyrolyzed at 900 and 1100 °C (Fig. 2a and Fig. S13) revealed that as the pyrolysis temperature increased, the intensity of the $FeN_{0.0324}$ phase peaks first increased and then decreased, while the Fe phase peaks continuously increased. This indicates that the lower pyrolysis temperatures (900 °C) hinder the complete formation of the $FeN_{0.0324}$ phase, while excessively high temperatures (1100 °C) promote its decomposition and Fe atom agglomeration, leading to a transformation to the more stable Fe phase. Thus, pyrolysis at 1000 °C favors the formation of a higher concentration of Fe-N_x sites in Fe-*N*-HOCNs. The defects and disordered structures of carbon material in the catalyst can also influence the electron transfer processes during the ORR process [30,31].

Raman spectroscopy was employed to analyze the graphitization degree of samples (Fig. S14a–b). The Raman spectra were deconvoluted into four components. The corresponding curve-fitting results, as well as

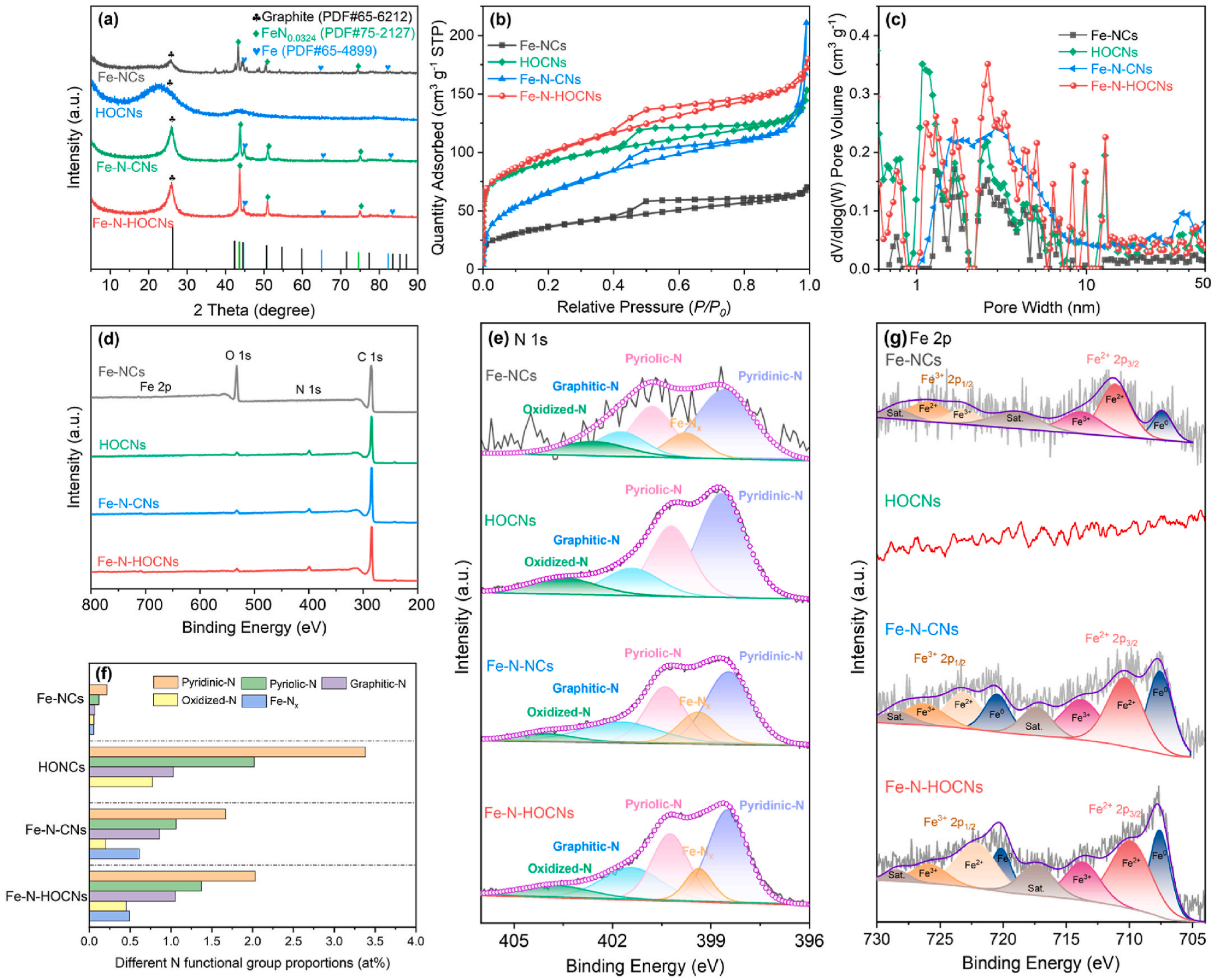

Fig. 2. (a) XRD patterns, (b) N_2 adsorption/desorption isotherms, (c) pore size distributions, (d) XPS survey spectra for the Fe-NCs, HOCNs, Fe-*N*-CNs, and Fe-*N*-HOCNs. (e) N 1s spectra, (f) the content of different nitrogen-containing functional groups, and (g) Fe 2p spectra for the Fe-NCs, HOCNs, Fe-*N*-CNs, and Fe-*N*-HOCNs.

the intensity ratio of the D and G bands (I_D/I_G). Generally, a higher I_D/I_G ratio reflects a greater degree of graphitization of the catalyst. Specifically, the I_D/I_G ratio of different samples (Fig. S14c–f), in ascending order, is 1.12 (HOCNs), 1.13 (Fe-*N*-HOCNs), 1.14 (Fe-*N*-CNs), and 1.22 (Fe-NCs). The degree of graphitization of Fe-NCs is the lowest, primarily due to its direct formation through the pyrolysis of FePc, during which the disordered stacking and transformation of FePc molecules lead to a higher density of structural defects. In contrast, the synthesis of HOCNs involves the ordered arrangement of PDA monomers along the specific crystal plane of S-1, which effectively suppresses the random nucleation and growth of carbon microcrystals in 3D space during pyrolysis, thereby exhibiting a higher degree of graphitization. Since Fe-*N*-HOCNs and HOCNs are synthesized in a similar manner, the introduction of FePc generates additional carbon defects, resulting in a slightly higher I_D/I_G ratio. Compared with Fe-*N*-HOCNs, Fe-*N*-CNs lacks the directional deposition of PDA during synthesis, and the incorporation of FePc further diminishes its graphitization degree. Furthermore, the I_D/I_G ratios of Fe-*N*-HOCNs-900 and Fe-*N*-HOCNs-1000 are 1.28 and 1.19, respectively (Fig. S14g–h). These results imply that the lower temperature (900 °C) constrains the graphitic transformation of the carbon layers. Conversely, an excessively high temperature (1100 °C) induces framework thinning and structural collapse, which in turn suppresses further improvement in the degree of graphitization and impedes efficient electron transport. Therefore, among the Fe containing samples, Fe-*N*-HOCNs maintains a relatively high degree of graphitization and structural stability, suggesting potentially better electrical conductivity.

N_2 adsorption/desorption isotherms of samples were examined, and the specific surface area and the porosity were analyzed by Brunauer-Emmett-Teller (BET) approach and non-local density functional theory (NLDFT) [32]. All the samples show the type IV isotherms containing a high adsorption capacity at $P/P_0 \leq 0.1$, suggesting their mesoporous and microporous composite structure (Fig. 2b) [33]. The pore size distribution curves are shown in Fig. 2c. Fe-*N*-HOCNs contains a large number of micro/mesopores with pore sizes of ~2 nm and 2~15 nm. The pore structure of Fe-*N*-HOCNs is similar to that of HOCNs, and the formation of internal micropores (<2 nm) and relatively small-sized mesopores (2~8 nm) is primarily attributed to the decomposition and transformation of FePc precursors during the pyrolysis process, as well as the framework shrinkage of PDA during its conversion into the carbon matrix. Meanwhile, Fe-*N*-HOCNs and HOCNs inherit the 8~15 nm mesoporous features from the S-1@HO-mPDA precursor, which originates from the synergistic self-assembly of P123 and F127 block copolymers, PDA precursors, and moderate TMB swelling agents during the synthesis stage [34]. Following high-temperature pyrolysis, the removal of the block copolymers accompanied by the thermal polycondensation and framework shrinkage of the PDA matrix, endows the materials with a highly permeable mesoporous structure. This is in agreement with the SEM and HRTEM observations. In contrast, Fe-*N*-CNs synthesized without the assistance of P123 and F127 fail to exhibit such a mesoporous structure. In addition, as shown in Table S1, the S_{BET} of Fe-*N*-HOCNs (354 $m^2 g^{-1}$) is larger than that of HOCNs (320 $m^2 g^{-1}$), Fe-*N*-CNs without hollow-out structure (250 $m^2 g^{-1}$), and Fe-NCs (120 $m^2 g^{-1}$). The V_{micro} and V_{micro}/V_{total} values of Fe-*N*-HOCNs (0.18 $cm^3 g^{-1}$, 64.3%) are significantly higher than those of Fe-NCs (0.07 $cm^3 g^{-1}$, 63.6%), HOCNs (0.14 $cm^3 g^{-1}$, 58.3%), Fe-*N*-CNs (0.11 $cm^3 g^{-1}$, 33.3%). The large S_{BET} and high micropore content in Fe-*N*-HOCNs are beneficial to the exposure of active sites in electrocatalytic reactions.

The metal element content, surface chemical composition, and valence states of samples were further characterized by using an inductively coupled plasma mass spectrometer (ICP-MS) and X-ray photoelectron spectroscopy (XPS). ICP-MS results indicated that the Fe content in Fe-NCs was 11.29 wt%, whereas the Fe content in Fe-*N*-CNs and Fe-*N*-HOCNs samples decreased to 4.04 wt% and 4.73 wt%, respectively (Fig. S15). This can be attributed to the acid washing treatment that both Fe-*N*-CNs and Fe-*N*-HOCNs have undergone, which effectively removes a significant number of unstable Fe species. Furthermore, during the matrix synthesis of Fe-*N*-HOCNs, the block copolymers can promote the formation of additional mesoporous structures within PDA. Under equivalent FePc molecules input, more mesoporous facilitates the encapsulation of more FePc molecules, thereby resulting in a slightly higher Fe content in Fe-*N*-HOCNs compared to Fe-*N*-CNs. The XPS spectra confirmed the presence of C (284.6 eV), N (399.1 eV), and O (532.2 eV) elements in all samples (Fig. 2d), indicating that the carbon layer contains a large amount of nitrogen [35]. Weak characteristic peaks of Fe 2p (709.1 eV) were observed in all samples except HOCNs, which can be attributed to iron compounds formed during the pyrolysis of FePc [36]. The C, N, and O contents (at%) of the samples are presented in Table S2. Due to the embedding of Fe species within the carbon structure, along with the influence of acid treatment and the limited detection depth of XPS, the specific content of the Fe element could not be detected on the sample surface. The N content on the surface of Fe-*N*-HOCNs (5.4 at%) is slightly higher than that of Fe-*N*-CNs (4.4 at%), inheriting the characteristic of HOCNs (7.2 at%). In Fig. 2e, the high-resolution N 1s spectra revealed nitrogen containing species, including pyridinic-N, pyrrolic-N, graphitic-N, and oxidized-N at binding energy of 398.4 eV, 400.2 eV, 410.4 eV, and 404.0 eV, respectively [37]. The Fe-N_x species at 399.4 eV

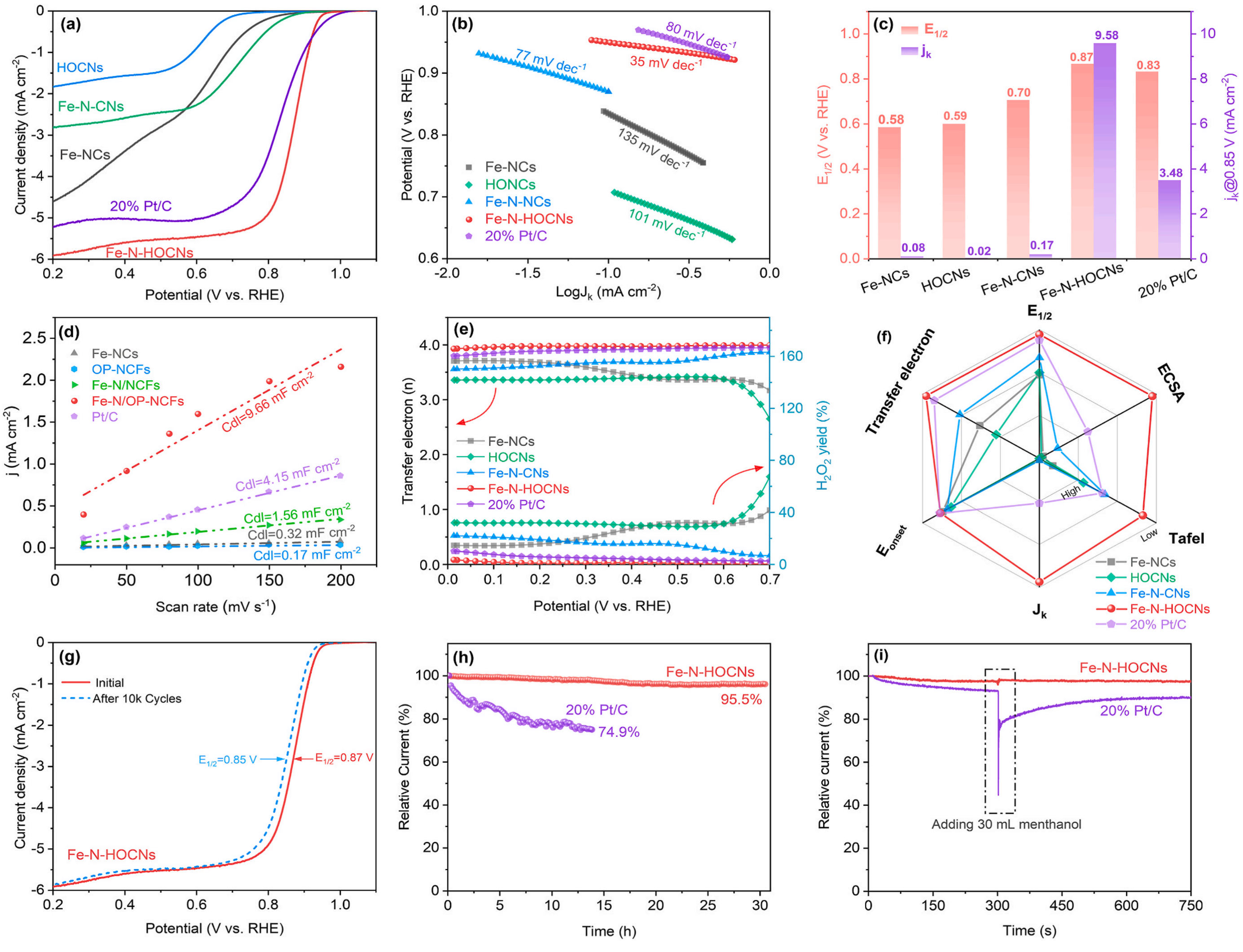

Fig. 3. (a) LSV curves, (b) Tafel plots, (c) half-wave potentials ($E_{1/2}$) and kinetic curves (j_k), (d) electrochemical double-layer capacitance (C_{dl}), (e) electron transfer numbers (n) and peroxide yield (H_2O_2%) of the Fe-NCs, HOCNs, Fe-*N*-CNs, Fe-*N*-HOCNs, and 20% Pt/C. (f) Radar plot on performance comparison with different ORR catalysts. (g) LSV curves of Fe-*N*-HOCNs before and after accelerated durability test (after 10k CV cycles). (h) Chronoamperometric responses and (i) methanol tolerance test of Fe-*N*-HOCNs, and 20% Pt/C with 30 mL methanol at 0.7 V and 1600 rpm in O_2-saturated 0.1 M KOH.

were detected in the Fe-NCs, Fe-*N*-CNs, and Fe-*N*-HOCNs samples [38, 39]. As shown in Fig. 3f, the atomic percentages of Fe-N_x species in Fe-*N*-HOCNs (0.59 at%) is similar to Fe-*N*-CNs (0.61 at%). This coordination between the metal and nitrogen atoms is considered an effective active site for ORR [40,41]. Moreover, both pyridinic-N and graphitic-N play critical roles in enhancing ORR activity. Pyridinic N can increase the delocalized π electrons in the carbon framework, enhancing nucleophilic attack on O_2. Graphitic nitrogen can promote O_2 adsorption, accelerate electron transfer, and increase the limiting current density [42,43]. In Fig. 2f, the nitrogen containing species of pyridinic-N (2.00 at%) and graphitic-N (1.05 at%) in Fe-*N*-HOCNs are higher than those in Fe-*N*-CNs (1.67 and 0.86 at%). The increase in nitrogen content, especially in pyridine-N and graphite-N, is beneficial to the improvement of catalytic performance. The Fe 2p spectra of Fe-NCs, Fe-*N*-CNs, and Fe-*N*-HOCNs reveal two significant peaks corresponding to Fe $2p_{1/2}$ (~723.0 eV) and Fe $2p_{3/2}$ (~710.0 eV), which are attributed to Fe^{3+} and Fe^{2+}, respectively [44]. The deconvoluted peaks centered around 710.0 eV and 722.2 eV correspond to Fe^{2+}, while the peaks located at approximately 713.7 eV and 725.9 eV are indicative of Fe^{3+}. Additionally, a prominent peak was observed at 707.5 eV, with a corresponding satellite at 720.1 eV, which is characteristic of Fe^0. Thus, the chemical valence states of Fe species in all Fe-NCs, Fe-*N*-CNs, and Fe-*N*-HOCNs composites range from Fe^0 to Fe^{3+} [45], which is consistent with the results of XRD. Based on the above results, Fe-*N*-HOCNs contains an abundance of pyridinic-N and graphitic-N, Fe-N_x sites, and bits of Fe nanoclusters. The presence of pyridinic-N and graphitic-N contributes to optimizing the electronic structure of the carbon matrix, while the Fe nanoclusters facilitate the disruption of the symmetrical electronic interface of Fe-N_x sites and the modulation of the Fe center's d orbitals [17,43]. The synergistic effect of multiple sites is expected to enhance the electron transfer path and improve the adsorption and desorption performance of oxygen-containing intermediate species, thereby increasing the intrinsic catalytic activity of the catalyst.

3.2. *Electrocatalytic performance of catalysts*

As shown in Fig. S16 of cyclic voltammetry (CV), Fe-*N*-HOCNs exhibits a more positive peak potential of ORR compared to other samples, indicating its excellent ORR catalytic activity. This result is further corroborated by the linear sweep voltammetry (LSV) curves derived from the rotating disk electrode (RDE) conducted at 1600 rpm in an O_2-saturated 0.1 M KOH (Fig. 3a). The Fe-*N*-HOCNs achieves a limiting current density of 5.9 mA cm^{-2}, superior to that of 20% Pt/C (5.2 mA cm^{-2}). It also exhibited a more positive half-wave potential ($E_{1/2} = 0.87$ V) compared to Pt/C ($E_{1/2} = 0.83$ V), while maintaining a comparable onset potential ($E_{\text{onset}} = 1.01$ V vs. 1.02 V for Pt/C), which are substantially better than the performance of Fe-NCs ($E_{1/2} = 0.58$ V, $E_{\text{onset}} = 0.99$ V), HOCNs ($E_{1/2} = 0.59$ V, $E_{\text{onset}} = 0.90$ V) and Fe-*N*-CNs ($E_{1/2} = 0.70$ V, $E_{\text{onset}} = 0.94$ V). Furthermore, Fe-*N*-HOCNs exhibit better catalytic activity relative to the samples prepared at other pyrolysis temperatures (Fig. S17). This superior performance is primarily ascribed to the modulation of phase evolution, microstructure, and graphitization degree by the pyrolysis temperature, which allows the catalyst to reach an optimal synergy between structural integrity and catalytic efficiency at 1000 °C. LSV tests were further performed at rotation speeds ranging from 400 to 2500 rpm (Fig. S18a–e). Based on the LSV results, the Koutecky-Levich (K-L) plots were constructed, exhibiting a robust linear relationship across various potentials (Fig. S18f–j), which confirms the first-class dynamics kinetics towards dioxygen fragmentation [46]. Furthermore, as shown in Fig. 3b, the kinetics of the Fe-*N*-HOCNs sample are evidenced by its lowest Tafel slope (35 mV dec^{-1}) compared to 20% Pt/C (80 mV dec^{-1}), Fe-NCs (135 mV dec^{-1}), HOCNs (101 mV dec^{-1}), and Fe-*N*-CNs (77 mV dec^{-1}). The lower Tafel slope indicates that the faster ORR kinetics, involving the processes of charge transfer, mass transport, utilization of active sites, etc. Additionally, the kinetic current density (j_k@0.85 V) of Fe-*N*-HOCNs was calculated to be 9.58 mA cm^{-2}, which is 2.75 times larger than that of 20% Pt/C and significantly higher than the other samples (Fig. 3c). More importantly, as shown in Table 1, the Fe-*N*-HOCNs has much higher mass activity (j_m, 658.17 mA mg_{Fe}^{-1}) and turnover frequency (TOF, 0.1160 e^- $site^{-1}$ s^{-1}) at 0.85 V in comparison with Fe-NCs (2.29 mA mg_{Fe}^{-1}, 0.0013 e^- $site^{-1}$ s^{-1}), Fe-*N*-CNs (13.98 mA mg_{Fe}^{-1}, 0.0081 e^- $site^{-1}$ s^{-1}) and 20% Pt/C (57.39 mA mg_{Pt}^{-1}, 0.1160 e^- $site^{-1}$ s^{-1}). The high j_m and TOF of Fe-*N*-HOCNs may be attributed to its more distinct microporous and mesoporous structure compared to Fe-NCs and Fe-*N*-CNs. In Fe-*N*-HOCNs, Fe sites (Fe-N_x and Fe clusters) are predominantly located in different pore regions of the micropores and mesopores within the carbon matrix. This spatial confinement effect reduces the size of the sites, and smaller-sized sites have a higher ratio of surface atoms to total atoms, thereby offering more electrocatalytic active sites [47]. Moreover, the confinement of Fe sites in distinct pore regions results in a heterogeneous spatial distribution, leading to strong interactions between Fe sites, which further enhances the catalytic efficiency of these sites [48]. The j_m and TOF provide strong evidence that Fe-*N*-HOCNs possess high intrinsic activity, and therefore could be expected to exhibit an excellent performance on accelerating ORR.

The electrochemically active surface area (ECSA) was evaluated by double-layer capacitance (C_{dl}) to reflect the accessible active sites. This goal was achieved by recording CV curves in the potential range of 0.95 V to 1.05 V at various scan rates. The CV curves for Fe-*N*-HOCNs, 20% Pt/C, and other samples at different scan rates are shown in Fig. S19. As shown in Fig. 3d, the calculated C_{dl} value for Fe-*N*-HOCNs is 9.66 mF cm^{-2}, which is significantly higher than those of Fe-NCs (0.32 mF cm^{-2}), HOCNs (0.17 mF cm^{-2}), Fe-*N*-CNs (1.56 mF cm^{-2}), and 20% Pt/C (4.15 mF cm^{-2}). This result suggests that the synergistic effect of accessible micro/mesoporous structure and highly dispersed Fe species in Fe-*N*-HOCNs enhances the exposure of electrochemically active sites. Meanwhile, the abundant nitrogen-containing functional groups are conducive to enhancing the surface wettability of the catalyst, facilitating the formation of gas-liquid-solid three-phase interfaces, which contributes to superior mass activity.

The electron transfer number (n) and H_2O_2 yield of the ORR process for Fe-*N*-HOCNs, 20% Pt/C, and other samples were measured and calculated by using a rotating ring-disk electrode (RRDE). As shown in Fig. 3e and Fig. S20, Fe-*N*-HOCNs exhibited the lowest H_2O_2 yield at 1.2%, with an electron transfer number close to 3.97, outperforming the 20% Pt/C (4.7%, 3.91). Its high selectivity for the four-electron ORR pathway and low yield of H_2O_2 by-products not only determine its high energy conversion efficiency, but also protect the catalyst from attacks by oxygen-containing radicals. The radar plot in Fig. 3f indicates that the Fe-*N*-HOCNs catalyst outperforms 20% Pt/C and other samples in terms of overall performance. When compared to previously reported Fe-based catalysts, the as-prepared Fe-*N*-HOCNs possesses good ORR activity and a high selectivity electron transfer pathway (Table S3).

Durability represents a crucial factor in evaluating commercial applications of catalysts. The accelerated durability test (ADT) was performed on both Fe-*N*-HOCNs and 20% Pt/C catalysts. The results showed that the $E_{1/2}$ of Fe-*N*-HOCNs decreased by only 20 mV after 10k CV cycles (Fig. 3g). In contrast, the $E_{1/2}$ of 20% Pt/C decreased by 50 mV after 10k CV cycles (Fig. S21). The chronoamperometry was utilized to further evaluate the durability of Fe-*N*-HOCNs (Fig. 3h). After approximately 30 h, the ORR current of Fe-*N*-HOCNs retains 95.5% of its initial

Table 1
Comparison of ORR performance for 20% Pt/C and prepared catalysts.

Samples	j_m (mA mg_{Fe}^{-1})	TOF (e^- $site^{-1}$ s^{-1})
Fe-NCs	2.29	0.0013
Fe-*N*-CNs	13.98	0.0081
Fe-*N*-HOCNs	658.17	0.3808
20% Pt/C	57.39	0.1160

value, demonstrating significantly better durability compared to 20% Pt/C, which retained only 74.9% of its initial current after 15 h. Fig. 3i shows the methanol tolerance test for Fe-*N*-HOCNs and 20% Pt/C. The relative current of Fe-*N*-HOCNs remained virtually unchanged after the introduction of methanol. In contrast, 20% Pt/C exhibited a substantial decrease in relative current upon methanol addition, and the current could not recover to its initial value. The above results indicate that Fe-*N*-HOCNs exhibits better durability and methanol tolerance compared to 20% Pt/C.

3.3. *Function of hollow-out structure*

To clarify the high intrinsic activity and excellent catalytic performance of Fe-*N*-HOCNs, electrochemical impedance spectroscopy (EIS) was firstly conducted on Fe-*N*-CNs and Fe-*N*-HOCNs at open-circuit potential. As shown in Fig. 4a, Nyquist plots exhibit two semicircles assigned to the charge-transfer process through electrode and electrolyte interfaces (high-frequency semicircle) and oxygen transfer in the cathode catalyst layer (low-frequency semicircle) [49]. As shown in Fig. S22, the charge-transfer resistance (R_{ct}) of Fe-*N*-HOCNs (1.54 Ω) is significantly lower than those for Fe-*N*-CNs (3.40 Ω). In Fe-*N*-HOCNs, electrons can be rapidly transferred along the framework of the hollow-out nitrogen-doped carbon nanoboxes, a structural feature absent in Fe-*N*-CNs. Additionally, Fe-*N*-HOCNs possess a higher degree of graphitization and more accessible active sites, further enhancing the electron transfer capability of Fe-*N*-HOCNs. With the decrease in frequency, the gap between the two samples gradually widened. Compared with Fe-*N*-HOCNs (82.1 Ω), the mass-transfer resistance (R_{mt}) of Fe-*N*-CNs sharply increases to 226.2 Ω, which is due to the difficult mass transfer in the Fe-*N*-CNs caused by the closed hollow-out structure. The distribution of relaxation times (DRT) was further applied to analyze the data obtained from the Nyquist plots. The DRT enables model-free impedance analysis without dependence on equivalent circuits [50]. In Fig. 4b, Fe-*N*-HOCNs and Fe-*N*-CNs exhibit three distinct peaks in the low-frequency (LF), intermediate-frequency (IF), and high-frequency (HF) regions, corresponding to oxygen mass transfer, charge transfer, and electronic conduction processes, respectively [51]. In the LF region, peak intensity of Fe-*N*-HOCNs is lower than Fe-*N*-CNs, further confirming that the hollow-out structure accelerated the mass transfer of O_2 during the ORR process. Additionally, the reduced peak intensities in the IF and HF regions for Fe-*N*-HOCNs also indicate superior electronic and charge transfer capabilities.

The electric double-layer capacitance was calculated according to EIS and CV to further quantitatively evaluate the influence of the porous structure [52]. As shown in Fig. 4c, the capacitance derived from the LF region in EIS mode, denoted as C_{dl}_EIS, represents the electrochemically wettable surface area under static conditions. Similarly, in CV mode (scan rate of 50 mV s^{-1}), the capacitance (C_{dl}_CV) reflects the electrochemical surface area under kinetic conditions. All of the C_{dl}_EIS and C_{dl}_CV for Fe-*N*-HOCNs (86.6 F g^{-1}, 57.6 F g^{-1}) are significantly much higher than those of Fe-*N*-CNs (16.3 F g^{-1}, 7.2 F g^{-1}). The results indicate that the unique hollow-out structure of Fe-*N*-HOCNs substantially enhances the charges accumulation and transfer. Meanwhile, the other two parameters were further introduced to evaluate accessibility [53]. The first parameter is the BET surface area-normalized C_{dl}_EIS (Fig. 4d). Assuming a uniform distribution of active sites, this value indicates the actual physical surface area involved in the electrochemical reaction. Compared with Fe-*N*-CNs (0.096 F m^{-2}), Fe-*N*-HOCNs has a higher C_{dl}_EIS/BET (0.245 F m^{-2}). This feature can be attributed to the hollow-out structure of Fe-*N*-HOCNs, which enables both the inner and outer surfaces of the carbon framework to be fully wetted by the electrolyte. As a result, the actual physical surface area involved in the electrochemical reaction is effectively increased. The contact angle of the Fe-*N*-CNs and Fe-*N*-HOCNs in the aqueous system also verified this result (Fig. S23). The second parameter is the ratio of C_{dl}_EIS to C_{dl}_CV (Fig. 4d), which is used to quantify the actual

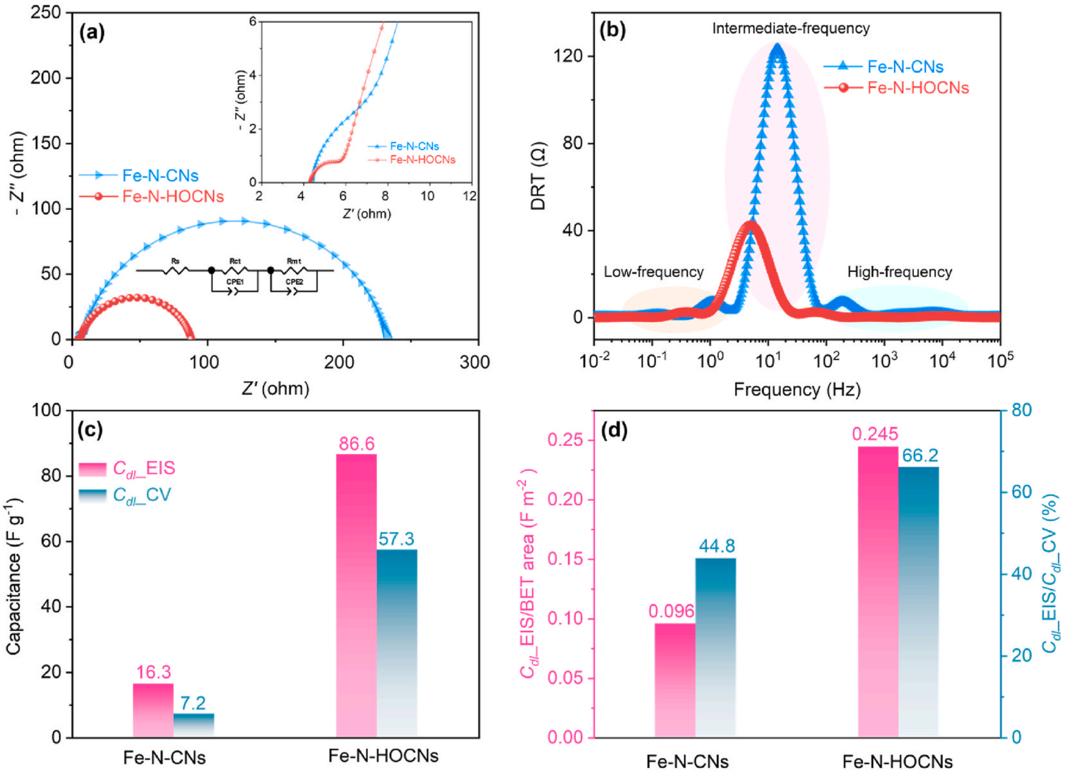

Fig. 4. (a) Nyquist plots via the RDE test, the inset displays the partially enlarged drawing and equivalent circuit model. (b) DRT of Fe-*N*-CNs and Fe-*N*-HOCNs. (c) Electric double-layer capacitance was calculated from EIS measured at OCP (C_{dl}_EIS) and CV measured at 50 mV s^{-1} (C_{dl}_CV) of Fe-*N*-CNs and Fe-*N*-HOCNs. (d) C_{dl}_EIS normalized by their S_{BET} of Fe-*N*-CNs and Fe-*N*-HOCNs, and the ratio between C_{dl}_EIS and C_{dl}_CV.

utilization efficiency of the electrode interface in ORR kinetics. The C_{dl}_EIS/C_{dl}_CV ratio for Fe-*N*-HOCNs (66.2%) is also higher than that for Fe-*N*-CNs (44.8%), further indicating that the unique hollow-out structure and penetrable micro/mesopores of Fe-*N*-HOCNs can effectively shorten the transport path of O_2, reduce diffusion resistance, and thus minimize kinetic barriers during mass transfer.

3.4. *Catalytic mechanism of active sites*

The coexistence of metal nanoclusters and *M*-N$_x$ species facilitates the modulation of their electronic structure and coordination environment, thereby reducing the energy barrier of the rate-determining step in the ORR process and enhancing the catalyst activity. This synergistic effect has been observed in various iron-based catalysts [54,55]. Building on the findings, DFT calculations were used to explore the influence mechanism of Fe-N$_x$ and Fe nanoclusters on ORR performance in Fe-*N*-HOCNs. Three model structures were constructed for the Fe active sites in Fe-*N*-HOCNs: a single Fe nanocluster in the carbon layer (Fe nanocluster), a single Fe-N$_4$ in the carbon layer (Fe-N$_x$), and Fe nanocluster/Fe-N$_4$ co-doped in the carbon layer (Fe nanocluster/Fe-N$_4$), which were designed to simulate the ORR process (Fig. 5a–c). It is worth noting that in the ORR process of the Fe nanocluster/Fe-N$_4$ model structure, a single O_2 molecule can be adsorbed in different adsorption sites: either on the Fe nanocluster or the Fe-N$_4$ site, denoted as Fe nanocluster*/Fe-N$_4$ and Fe nanocluster/Fe-N$_4$*, respectively. The optimized structures of all models, along with their adsorbed intermediates, are shown in Fig. S24. The Gibbs free energy of the optimized intermediate species (*O_2, *OOH, *O, and *OH) catalytic sites is provided in Fig. 5d and Table S4. The rate-determining step for all models is the final reduction step of *OH + e^- = * + OH^-. The ORR overpotential of Fe nanocluster*/Fe-N$_4$ (0.49 V) and Fe cluster/Fe-N$_4$* (0.48 V) is similar and markedly lower than that of Fe cluster* (0.73 V) and Fe-N* (0.78 V), confirming that the coexistence of Fe nanocluster and Fe-N$_x$ in Fe-*N*-HOCNs can significantly enhance ORR activity. This enhancement could be attributed to the *OH adsorption energy of the Fe nanocluster*/Fe-N$_4$ (−1.11 eV) and Fe nanocluster/Fe-N$_4$* (−1.05 eV) fall within an intermediate range (Fig. 5e), between the single Fe nanocluster* (−1.24 eV) and the single Fe-N$_4$* (−0.87 eV). The Fe-*N*-HOCNs possessing moderate adsorption capabilities, effectively prevent from desorption barriers caused by excessive intermediate adsorption, while also avoid the loss of catalytic efficiency associated with overly weak adsorption.

Moreover, DOS near the Fermi level is closely linked to the electrical conductivity of materials, with a higher DOS value typically corresponding to better conductivity [56–58]. As shown in Fig. 5f, the DOS value of Fe nanocluster/Fe-N$_4$ model is 22.12/eV, it is much higher than the Fe nanocluster (3.36/eV) and Fe-N$_4$ (6.27/eV) models, indicating its superior conductivity. Since the Fe-N$_4$ site modulates local charge distribution and facilitates the transfer of π-electrons in the carbon layer to the numerous unoccupied 3d orbitals of the Fe nanocluster, thereby strengthening the interaction between the d and π orbitals. Meanwhile, the Fe-N$_4$ site induces electron rearrangement in regions distant from the Fe nanoclusters, thereby expanding the spatial range of coupling to

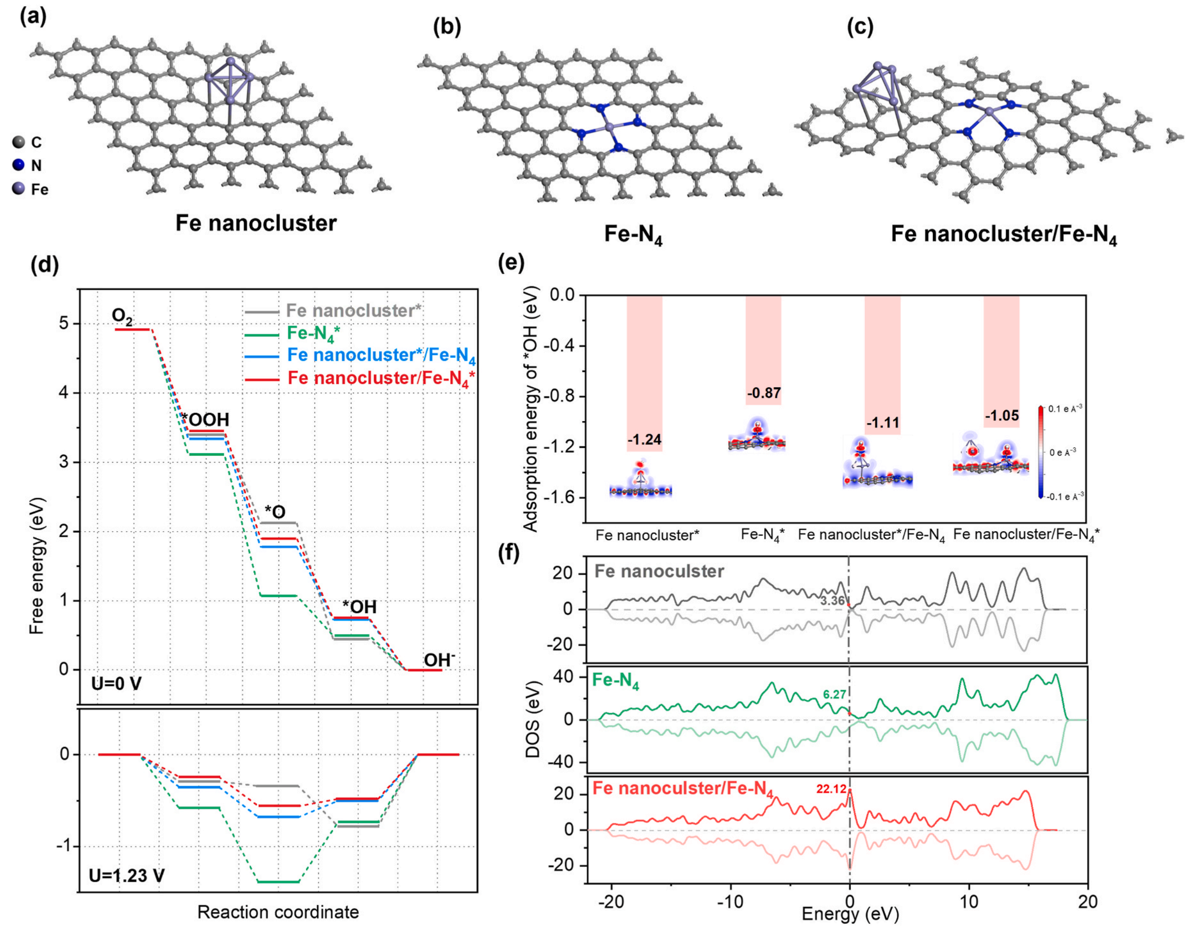

Fig. 5. DFT calculations elucidating the activities of the three model structures: (a) Fe nanocluster, (b) Fe-N$_4$, and (c) Fe nanocluster/Fe-N$_4$. The single Fe nanocluster or Fe-N$_4$ each has a single adsorption active site, labeled as Fe nanocluster* or Fe-N$_4$*, respectively. The Fe nanocluster/Fe-N$_4$ structure possesses two adsorption active sites, denoted as Fe nanocluster*/Fe-N$_4$ and Fe nanocluster/Fe-N$_4$*. (d) Gibbs free energy profiles for the ORR at U = 0 and 1.23 V. (e) The adsorption energies and charge density of *OH intermediates on different model structures. Densities are displayed with an isosurface, and the interval of isovalue is between −0.1 and 0.1 e/Å^3. (f) The density of states (DOS) of three model structures for Fe nanocluster, Fe-N$_4$, and Fe nanocluster/Fe-N$_4$.

enable broader participation of π-electrons in coupling with the 3d orbitals of the Fe atom, which enhances the electrical conductivity. Consequently, the theoretical calculations suggest that the coexistence of Fe nanoclusters and Fe-N_4 sites in Fe-*N*-HOCNs provides moderate intermediate adsorption capability and enhances the electronic conductivity, thereby imparts a smartly intrinsic activity of Fe-*N*-HOCNs toward ORR.

3.5. Zn-air batteries measurements

To validate the feasibility of the Fe-*N*-HOCNs catalyst in practical applications, the finite element simulation is firstly employed to evaluate the O_2 transport behavior of Fe-*N*-HOCNs and Fe-*N*-CNs in CCL under conditions close to actual working scenarios. The 2D and 3D models of the Fe-*N*-HOCNs catalyst exhibit a quasi-rectangular shape with lateral and central hollow-out structures, whereas the 2D and 3D models of the Fe-*N*-CNs catalyst are solid quasi-rectangles without hollow-out structure. The impact of lateral pore structures in Fe-*N*-HOCNs on O_2 transport was evaluated using a 2D model. Assuming the CCL made from Fe-*N*-HOCNs has the same thickness as that of Fe-*N*-CNs, the CCL consists of closely packed quadrilaterals. Fig. 6a shows the time-dependent O_2 distribution in different samples. Under the same time gradient, the O_2 concentration in the CCL of Fe-*N*-HOCNs was significantly higher than Fe-*N*-CNs. The CCL of Fe-*N*-HOCNs takes only 30 m s to be fully saturated with oxygen, which is far superior to Fe-*N*-CNs. The 3D model further evaluated the influence of the central hollow-out structure on the O_2 transport. As shown in Fig. 6b, the O_2 filling rate of Fe-*N*-HOCNs remains higher than Fe-*N*-CNs. Based on simulation results, Fe-*N*-HOCNs exhibit a faster O_2 transport rate when applied in CCL structure. Fe-*N*-HOCNs feature a unique 3D hollow-out nanoboxes with lateral and central hollow structures, which can significantly facilitate the O_2 transport and prevents the phenomenon of partial O_2 molecule transport from being hindered due to blocked transport channels commonly observed in traditional nanoparticle-like catalysts such as Fe-*N*-NCs (Fig. 6c). Additionally, the gas diffusion layers loaded with catalysts were characterized by SEM. As shown in Fig. S25, the catalytic layer of Fe-*N*-HOCNs provides significantly more abundant gas transport channels and space compared to Fe-*N*-CNs that lacks pore structure resulting a densely packed particle arrangement.

Based on the advantages in structure and catalytic performance, Fe-*N*-HOCNs was applied to primary zinc-air batteries (ZABs), in which a polished Zn plate with a thickness of 0.2 mm and the Fe-*N*-HOCNs

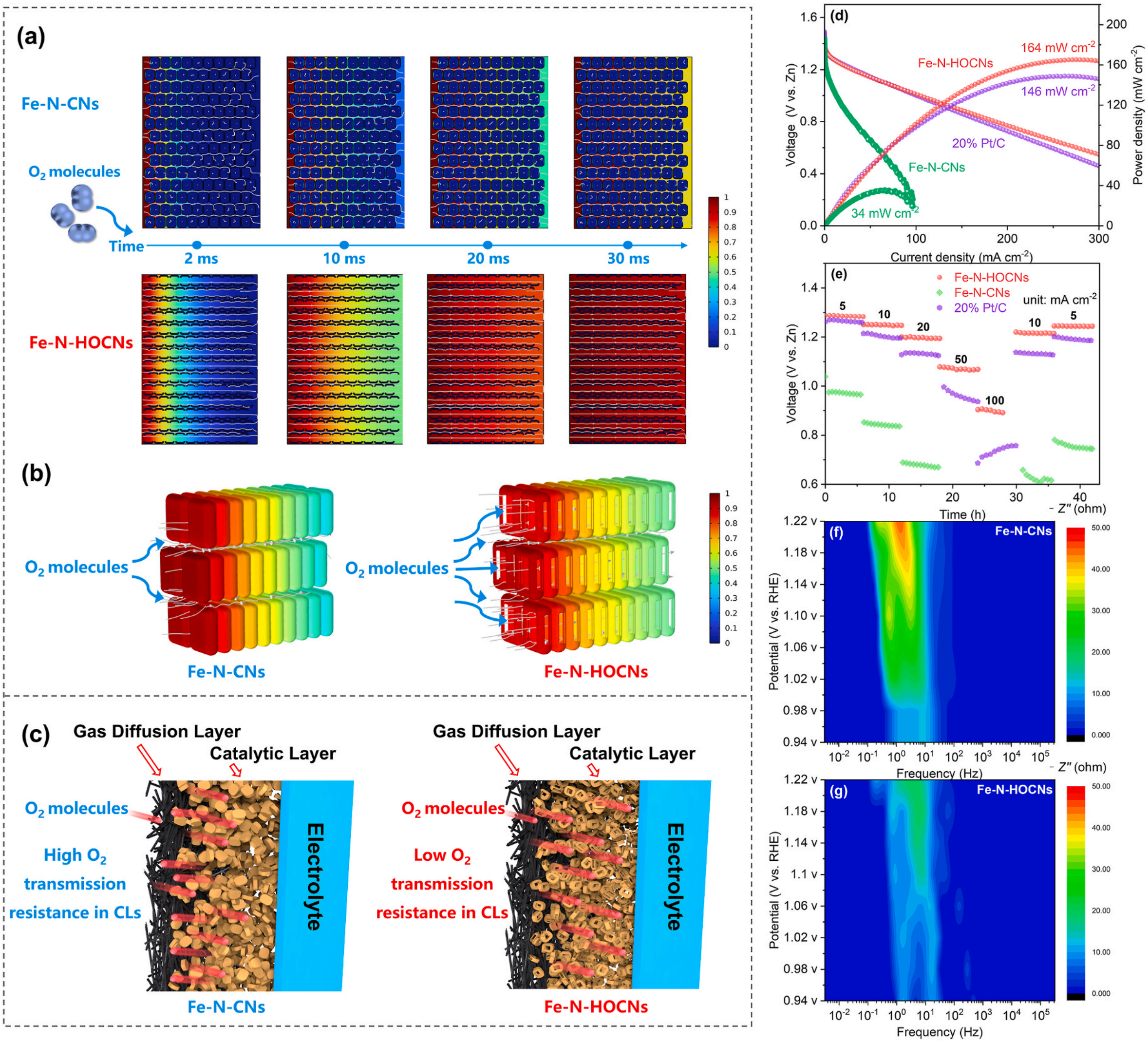

Fig. 6. (a) 2D models and (b) 3D models with time of Fe-*N*-CNs and Fe-*N*-HOCNs. (c) Schematic illustration of the local environment in the membrane electrode assembly, emphasizing the porous CCL of Fe-*N*-HOCNs and the solid CCL of Fe-*N*-CNs (red ball represents O_2). (d) Polarization and power density curves of ZABs with 6 M KOH+0.2 M $(CH_3COO)_2Zn$ electrolyte (scan rate: 5 mV s^{-1}), and (e) discharge curves of ZABs at different current densities using Fe-*N*-CNs, Fe-*N*-HOCNs and 20% Pt/C as ORR catalysts. 2D contour plot of the in situ distribution of relaxation times for catalysts (f) Fe-*N*-CNs and (g) Fe-*N*-HOCNs. (For interpretation of the references to color in this figure legend, the reader is referred to the Web version of this article.)

catalyst-loaded carbon paper was respectively used as the anode and the air cathode, and 6.0 M KOH/0.2 M $(CH_3COO)_2Zn$ was used as an electrolyte (Fig. S26). As shown in Fig. S27, the Fe-*N*-HOCNs-based ZAB has an open-circuit potential (OCP) of 1.55 V, substantially surpassing that of Fe-*N*-CNs (1.37 V) and 20% Pt/C (1.43 V). Discharge polarization curves and corresponding power density profiles (Fig. 6d) further highlighted the superiority of ZAB with Fe-*N*-HOCNs, delivering a peak power density of 164 mW cm^{-2} compared to 20% Pt/C (146 mW cm^{-2}) and Fe-*N*-CNs (34 mW cm^{-2}). Furthermore, the gravimetric specific capacity calculated from zinc consumption reached 774 mAh g^{-1} for the ZAB with Fe-*N*-HOCNs (Fig. S28), exceeding ZAB with the 20% Pt/C (760 mAh g^{-1}) and Fe-*N*-CNs (737 mAh g^{-1}). The rate performance was systematically evaluated through galvanostatic discharge tests (Fig. 6e). The ZAB with Fe-*N*-HOCNs outputs voltages of 1.29 V at 5 mA cm^{-2}, 1.07 V at 50 mA cm^{-2}, and 0.90 V at 100 mA cm^{-2}, which significantly outperforms the ZAB with Pt/C (1.27, 0.99, and 0.75 V under identical conditions) and Fe-*N*-CNs (0.96 V and 0.75 V at 5 and 50 mA cm^{-2}, respectively). Remarkably, the voltage recovered to 1.25 V upon the current returning to 5 mA cm^{-2}, showcasing outstanding rate resilience for the ZAB with Fe-*N*-HOCNs. Furthermore, the long-term durability of the Fe-*N*-HOCNs-based ZAB was evaluated through galvanostatic charge-discharge cycling tests (Fig. S29) at a current density of 5 mA cm^{-2}. The ZAB maintained stable operation for over 150 h, underscoring its significant potential for practical applications.

To gain deeper insights into the O_2 transport characteristics in the ZABs, in situ EIS analysis was conducted over the discharge voltage range of 0.94-1.22 V. Fig. S30a demonstrates that ZAB equipped with Fe-*N*-HOCNs catalysts exhibit significantly lower the impedance across the entire potential window than the ZAB using Fe-*N*-CNs as catalyst. The impedance data were deconvoluted via DRT analysis (Fig. S30b), the DRT values of the Fe-*N*-HOCNs ZAB system at LF and IF regions under different potentials were always lower than those of Fe-*N*-CNs. Converting the in-situ DRT analysis results into a 2D contour plots can more intuitively reveal the dynamic spatial distribution of DRT values (Fig. 6e and f). The Fe-*N*-HOCNs ZAB system consistently exhibits a low DRT value in the LF impedance (0.1-10 Hz) across different voltages, attributing to the 3D interconnected channels formed by the hollow-out nanoboxes structure that effectively reduce the O_2 transport resistance. In the IF range (10-1000 Hz), the impedance slightly increased with voltage may be due to the accelerated ORR at higher potentials, leading to an increased generation of intermediates that partially accumulate on the active site surfaces to hinder ion transport in subsequent reactions [59]. In contrast, the impedance of ZAB with Fe-*N*-CNs significantly increases from LF to IF as the voltage increases. This phenomenon indicates that the limited mass transport pathways within Fe-*N*-CNs are insufficient to meet reaction requirements, resulting in a mismatch between O_2 transport and electrochemical reaction rates.

4. Conclusion

In summary, by employing a region-selective deposition strategy, we successfully synthesized a catalyst of Fe-*N*-HOCNs featuring that a hollow-out carbon nanoboxes structure incorporates Fe-N_x sites and Fe nanoclusters. The unique hollow-out and penetrable porous structure enhances the transport and accessibility of O_2 to the complex active sites of Fe-N_x and Fe nanoclusters, resulting a superior catalytic efficiency on ORR of Fe-*N*-HOCNs. Despite Fe containing only 4.73 wt%, the Fe-*N*-HOCNs exhibited an $E_{1/2}$ of 0.87 V (vs. RHE), a high limiting current density (5.9 mA cm^{-2}) and an excellent mass activity (658.17 mA mg_{Fe}^{-1}). DFT calculations suggest that the coexistence of Fe-N_x and Fe nanoclusters optimizes the binding strength of reaction intermediates and the electronic transfer ability of active sites, thereby reducing the ORR overpotential. Finite element simulations further indicate that the hollow-out structure significantly promotes O_2 transport within the catalyst layer, ensuring a high concentration of O_2 inside Fe-*N*-HOCNs during ORR. The power density of the ZAB, employing Fe-*N*-HOCNs as the air cathode, achieved 164 mW cm^{-2}, along with high specific capacity (774 mAh g_{Zn}^{-1}) and good rate performance. In situ EIS measurements and DRT analysis further demonstrate the small O_2 transport resistance of Fe-*N*-HOCNs in ZAB. This work offers a novel reference into the design and optimization of high-efficiency ORR catalysts by simultaneously enhancing the intrinsic catalytic activity and utilization rate of active sites and effectively utilizing them in the catalyst layer.

CRediT authorship contribution statement

Zheyan Tang: Writing – original draft, Methodology, Formal analysis, Data curation. **Hongwei Zhao:** Writing – review & editing, Methodology, Funding acquisition, Data curation. **Lin Tao:** Software, Methodology. **Wenhao Liu:** Methodology. **Lixiang Li:** Writing – review & editing, Funding acquisition. **Yutong Shi:** Methodology. **Jingang Zheng:** Methodology. **Lin Wu:** Methodology, Data curation. **Han Zhang:** Supervision, Methodology. **Fang Di:** Supervision, Data curation. **Chengguo Sun:** Supervision. **Zhihao Yao:** Software. **Yanzhou Qin:** Software. **Baigang An:** Writing – review & editing, Supervision, Resources, Methodology, Funding acquisition, Data curation.

Declaration of competing interest

The authors declare that they have no known competing financial interests or personal relationships that could have appeared to influence the work reported in this paper.

Acknowledgements

We acknowledge the financial support by grants from the National Natural Science Foundation of China (52371224, 51872131, 51972156), the Startup Fund for Doctoral Research of Liaoning (2023-BS-184), the University of Science and Technology Liaoning Talent Project Grants (6003000315), the Fundamental Research Funds for the Liaoning Universities (LJ222410146062, LJ212410146075). The authors extend their gratitude to the Theoretical and Computational Chemistry Team from Shiyanjia Lab (www.shiyanjia.com) for providing invaluable assistance.

Appendix A. Supplementary data

Supplementary data to this article can be found online at https://doi.org/10.1016/j.ijhydene.2026.154698.

References

[1] Tian X, Lu X, Xia B, Lou X. Advanced electrocatalysts for the oxygen reduction reaction in energy conversion technologies. Joule 2020;4:45–68. https://doi.org/10.1016/j.joule.2019.12.014.

[2] Zhang Q, Guan J. Applications of atomically dispersed oxygen reduction catalysts in fuel cells and zinc–air batteries. Energy Environ Mater 2020;4:307–35. https://doi.org/10.1002/eem2.12128.

[3] Zhou W, Su H, Cheng W, Li Y, Jiang J, Liu M, Yu F, Wang W, Wei S, Liu Q. Regulating the scaling relationship for high catalytic kinetics and selectivity of the oxygen reduction reaction. Nat Commun 2022;13:6414. https://doi.org/10.1038/s41467-022-34169-w.

[4] Yang K, Su Y, Xu C, Guo P, Zhao Y, Liu X, Jia L, Yang Y, Zhu H, Wei P, Liu J. Boosting oxygen reduction reaction through substrate fluorination-mediated d-band center tuning and microenvironment optimization of molecular catalysts. ACS Catal 2025;15:8114–24. https://doi.org/10.1021/acscatal.5c00880.

[5] Kodama K, Nagai T, Kuwaki A, Jinnouchi R, Morimoto Y. Challenges in applying highly active Pt-based nanostructured catalysts for oxygen reduction reactions to fuel cell vehicles. Nat Nanotechnol 2021;16:140–7. https://doi.org/10.1038/s41565-020-00824-w.

[6] Jia F, Li P, Mao D, Chen H, Li Z. Tuning electrocatalytic activity of Janus CrSSe via TM atom adsorption: implications for HER/HOR/ORR/OER reactions. Int J Hydrogen Energy 2025;180:151778. https://doi.org/10.1016/j.ijhydene.2025.151778.

[7] Zhao H, Xing T, Li L, Geng X, Guo K, Sun C, Zhou W, Yang H, Song R, An B. Synthesis of cobalt and nitrogen co-doped carbon nanotubes and its ORR activity as the catalyst used in hydrogen fuel cells. Int J Hydrogen Energy 2019;44:25180–7. https://doi.org/10.1016/j.ijhydene.2019.03.271.

[8] Li R, Li X, Liu Q, Yue H, Meng Y, Tian Y. Effect of Fe–N–C single atom/cluster catalyst on ORR of PEMFC. Int J Hydrogen Energy 2025;139:718–29. https://doi.org/10.1016/j.ijhydene.2025.05.294.

[9] Liu S, Li C, Zachman M, Zeng Y, Yu H, Li B, Wang M, Braaten J, Liu J, Meyer H, Lucero M, Kropf A, Alp E, Gong Q, Shi Q, Feng Z, Xu H, Wang G, Myers D, Xie J, Cullen D, Litster S, Wu G. Atomically dispersed iron sites with a nitrogen–carbon coating as highly active and durable oxygen reduction catalysts for fuel cells. Nat Energy 2022;7:652–63. https://doi.org/10.1038/s41560-022-01062-1.

[10] Liu M, Zhang J, Su H, Jiang Y, Zhou W, Yang C, Bo S, Pan J, Liu Q. In situ modulating coordination fields of single-atom cobalt catalyst for enhanced oxygen reduction reaction. Nat Commun 2024;15:1675. https://doi.org/10.1038/s41467-024-45990-w.

[11] Dai Y, Liu B, Zhang Z, Guo P, Liu C, Zhang Y, Zhao L, Wang Z. Tailoring the d-orbital splitting manner of single atomic sites for enhanced oxygen reduction. Adv Mater 2023;35:2210757. https://doi.org/10.1002/adma.202210757.

[12] Zeng Y, Wang X, Qi W, Liu C, Lu L, Xiao M, Li K, Xiao F, Shao M, Xing W, Zhu J. Aligned d-orbital energy level of dual-atom sites catalysts for oxygen reduction reaction in anion exchange membrane fuel cells. Nat Commun 2025;16:8111. https://doi.org/10.1038/s41467-025-63322-4.

[13] Mun Y, Lee S, Kim K, Kim S, Lee S, Han J, Lee J. Versatile strategy for tuning ORR activity of a single Fe-N_4 site by controlling electron-withdrawing/donating properties of a carbon plane. J Am Chem Soc 2019;141:6254–62. https://doi.org/10.1021/jacs.8b13543.

[14] Lu X, Li Y, Yang P, Wan Y, Wang D, Xu H, Liu L, Xiao L, Li R, Wang G, Zhang J, An M, Wu G. Atomically dispersed Fe-N-C catalyst with densely exposed Fe-N_4 active sites for enhanced oxygen reduction reaction. Chem Eng J 2024;485: 149529. https://doi.org/10.1016/j.cej.2024.149529.

[15] Zong L, Fan K, Cui L, Lu F, Liu P, Li B, Feng S, Wang L. Constructing Fe-N_4 sites through anion exchange-mediated transformation of Fe coordination environments in hierarchical carbon support for efficient oxygen reduction. Angew Chem Int Ed 2023;62:e202309784. https://doi.org/10.1002/anie.202309784.

[16] Wan X, Liu Q, Liu J, Liu S, Liu X, Zheng L, Shang J, Yu R, Shui J. Iron atom-cluster interactions increase activity and improve durability in Fe-N-C fuel cells. Nat Commun 2022;13:2963. https://doi.org/10.1038/s41467-022-30702-z.

[17] Wang Z, Lu Z, Ye Q, Yang Z, Xu R, Kong K, Zhang Y, Yan T, Liu Y, Pan Z, Huang Y, Lu X. Construction of Fe nanoclusters/nanoparticles to engineer FeN_4 sites on multichannel porous carbon fibers for boosting oxygen reduction reaction. Adv Funct Mater 2024;34:2315150. https://doi.org/10.1002/adfm.202315150.

[18] Ma R, Lin G, Zhou Y, Liu Q, Zhang T, Shan G, Yang M, Wang J. A review of oxygen reduction mechanisms for metal-free carbon-based electrocatalysts. npj Comput Mater 2019;5:78. https://doi.org/10.1038/s41524-019-0210-3.

[19] Liang C, Zhang T, Sun S, Han A, Qiu Z, Xu H, Liu J. Yolk-shell FeCu/NC electrocatalyst boosting high-performance zinc-air battery. Nano Res 2024;17: 7918–25. https://doi.org/10.1007/s12274-024-6766-3.

[20] Malko D, Kucernak A, Lopes T. In situ electrochemical quantification of active sites in Fe–N/C non-precious metal catalysts. Nat Commun 2016;7:13285. https://doi.org/10.1038/ncomms13285.

[21] Jiang Z, Liu X, Liu X, Huang S, Liu Y, Yao Z, Zhang Y, Zhang Q, Gu L, Zheng L, Li L, Zhang J, Fan Y, Tang T, Zhuang Z, Hu J. Interfacial assembly of binary atomic metal-N_x sites for high-performance energy devices. Nat Commun 2023;14:1822. https://doi.org/10.1038/s41467-023-37529-2.

[22] Ma FX, Zhang G, Wang M, Liang X, Lyu F, Xiao X, Wang P, Zhen L, Lu J, Zheng L, Yang Li Y, Xu CY. Encapsulating atomic molybdenum into hierarchical nitrogen-doped carbon nanoboxes for efficient oxygen reduction. J Colloid Interface Sci 2022;620:67–76. https://doi.org/10.1016/j.jcis.2022.04.002.

[23] Ma FX, Wu J, Liang X, Zhang G, Liu ZQ, Fan HS, Lu J, Xu CY, Zeng XC, Li YY. Axial orbital hybridization enables single-atom Fe-N-C hollow microplates for efficient oxygen reduction. Sci China Mater 2026;69:930–9. https://doi.org/10.1007/s40843-025-3682-6.

[24] Chen G, Han J, Niu Z, She P, Li L, Guan B, Yu J. Regioselective surface assembly of mesoporous carbon on zeolites creating anisotropic wettability for biphasic interface catalysis. J Am Chem Soc 2023;145:9021–8. https://doi.org/10.1021/jacs.3c00309.

[25] Chen G, She P, Han J, Li J, Tian G, Sun Y, Gao Y, Yang G, Diao Z, Guan B, Yu J. Structurally engineering multi-shell hollow zeolite single crystals via defect-directed oriented-kinetics transformation and their heterostructures for hydrideoxygenation reaction. Angew Chem Int Ed 2025;64:e202424690. https://doi.org/10.1002/anie.202424690.

[26] Xie Y, Sun F, Chang K, Li G, Song Z, Huang J, Cheng X, Zhuang G, Kuang Q. Axially coordinated gold nanoclusters tailoring Fe-N-C nanozymes for enhanced oxidase-like specificity and activity. Adv Sci 2024;11:2306911. https://doi.org/10.1002/advs.202306911.

[27] Li G, Sheng K, Lei Y, Yang J, Chen Y, Guo X, Chen G, Chang B, Wu T, Wang X. Facile synthesis of Fe_3C-dominated Fe/Fe_3C/$FeN_{0.0324}$ multiphase nanocrystals embedded in nitrogen-modified graphitized carbon as efficient pH-universal catalyst for oxygen reduction reaction and zinc-air battery. Chem Eng J 2023;451: 138823. https://doi.org/10.1016/j.cej.2022.138823.

[28] Luo R, Wang R, Meng Z, Xia Y, Tang H. Dysprosium-induced $FeN_{0.0324}$-Dy_2O_3 sites with efficient bifunctional oxygen electrocatalytic reactions for Zn-air batteries. Adv Compos Hybrid Mater 2023;6:5. https://doi.org/10.1007/s42114-023-00685-6.

[29] Lin W, Lin H, Chen H, Hwu Y, Chiou Y, Hong H. Shape effects of iron nanowires on hyperthermia treatment. J Nanomater 2013;2013:237439. https://doi.org/10.1155/2013/237439.

[30] Li Y, Liu Q, Zhang S, Li G. The vital balance of graphitization and defect engineering for efficient bifunctional oxygen electrocatalyst based on N-doping Carbon/CNT frameworks. ChemCatChem 2019;11:861–7. https://doi.org/10.1002/cctc.201801678.

[31] Huang Q, Xu S, Liu J, Guo Y, Chen D, Sun Q, Zhang L, Nie H, Yang Z, Qian J. Fe phthalocyanine stabilized on phosphorous-doped multi-defective carbon nanoribbons as oxygen reduction electrocatalysts. Appl Catal B Environ 2023;339: 123172. https://doi.org/10.1016/j.apcatb.2023.123172.

[32] Baldovino-Medrano V, Niño-Celis V, Isaacs Giraldo R. Systematic analysis of the nitrogen adsorption-desorption isotherms recorded for a series of materials based on microporous-mesoporous amorphous aluminosilicates using classical methods. J Chem Eng Data 2023;68:2512–28. https://doi.org/10.1021/acs.jced.3c00257.

[33] Zhao H, Chen Y, Zuo H, Li L, Li L, Ai F, Tang Z, Xing T, Zhang Y, Tao L, Tian Z, Yang H, Geng X, An B. Enhanced activity and durability of Pt nanoclusters catalyst by using nitrogen-doped carbon layer coated carbon nanotubes as anchors and nanowires for ORR. Catal Today 2024;438:114811. https://doi.org/10.1016/j.cattod.2024.114811.

[34] Wu W, Zhang W, Long Y, Qin J, Ma J. MOF-derived Fe-N-C with interconnected mesoporous structure for halonitrobenzenes hydrogenation: role of dicyandiamide on the growth of active sites and pore structure. Microporous Mesoporous Mater 2021;328:111472. https://doi.org/10.1016/j.micromeso.2021.111472.

[35] Ayiania M, Smith M, Hensley A, Scudiero L, McEwen J, Garcia-Perez M. Deconvoluting the XPS spectra for nitrogen-doped chars: an analysis from first principles. Carbon 2020;162:528–44. https://doi.org/10.1016/j.carbon.2020.02.065.

[36] Liu Y, Fan Y, Liu Z. Pyrolysis of iron phthalocyanine on activated carbon as highly efficient non-noble metal oxygen reduction catalyst in microbial fuel cells. Chem Eng J 2019;361:416–27. https://doi.org/10.1016/j.cej.2018.12.105.

[37] Lazar P, Mach R, Otyepka M. Spectroscopic fingerprints of graphitic, pyrrolic, pyridinic, and chemisorbed nitrogen in N-doped graphene. J Phys Chem C 2019; 123:10695–702. https://doi.org/10.1021/acs.jpcc.9b02163.

[38] He Y, Shi Q, Shan W, Li X, Kropf A, Wegener E, Wright J, Karakalos S, Su D, Cullen D, Wang G, Myers D, Wu G. Dynamically unveiling metal-nitrogen coordination during thermal activation to design high-efficient atomically dispersed CoN_4 active sites. Angew Chem Int Ed 2021;60:9516–26. https://doi.org/10.1002/anie.202017288.

[39] Liu Q, Li Y, Zheng L, Shang J, Liu X, Yu R, Shui J. Sequential synthesis and active-site coordination principle of precious metal single-atom catalysts for oxygen reduction reaction and PEM fuel cells. Adv Energy Mater 2020;10:2000689. https://doi.org/10.1002/aenm.202000689.

[40] Lu F, Fan K, Cui L, Li B, Yang Y, Zong L, Wang L. Engineering FeN_4 active sites onto nitrogen-rich carbon with tubular channels for enhanced oxygen reduction reaction performance. Appl Catal B Environ 2022;313:121464. https://doi.org/10.1016/j.apcatb.2022.121464.

[41] Kim J, Sa Y, Jeong H, Joo S. Roles of Fe-N_x and Fe-Fe_3C@C species in Fe-N/C electrocatalysts for oxygen reduction reaction. ACS Appl Mater Interfaces 2017;9: 9567–75. https://doi.org/10.1021/acsami.6b13417.

[42] Ye B, Tang H, Liu Q, Wang W, Wang L, Hu J. Extended π-conjugated system in carbon nitride by incorporating pyridine rings and N vacancies for photocatalytic H_2 evolution and H_2O_2 production. Carbon 2023;204:465–74. https://doi.org/10.1016/j.carbon.2022.12.075.

[43] Li G, Deng W, He L, Wu J, Liu J, Wu T, Wang Y, Wang X. Zn, Co, and Fe tridoped N-C core-shell nanocages as the high-efficiency oxygen reduction reaction electrocatalyst in zinc-air batteries. ACS Appl Mater Interfaces 2021;13:28324–33. https://doi.org/10.1021/acsami.1c06750.

[44] Serra A, Dhingra A, Asensio M, Real J, Royo J. Surface stabilisation of the high-spin state of Fe(ii) spin-crossover complexes. Phys Chem Chem Phys 2023;25: 14736–41. https://doi.org/10.1039/d3cp00863k.

[45] Niu W, Li R, Zhao W, Yan Y, Feng E, Chen J, Gu B, Liu M, Chueh Y. Hierarchical porous Fe-N/C@surfactant composites synthesized by a surfactant-assisted strategy as high-performance bifunctional oxygen electrodes for rechargeable zinc-air batteries. J Colloid Interface Sci 2023;649:435–44. https://doi.org/10.1016/j.jcis.2023.06.127.

[46] Wang J, Zhao C, Liu J, Ren D, Li B, Huang J, Zhang Q. Quantitative kinetic analysis on oxygen reduction reaction: a perspective. Nano Mater Sci 2021;3:313–8. https://doi.org/10.1016/j.nanoms.2021.03.006.

[47] Ma Q, Jin H, Zhu J, Li Z, Xu H, Liu B, Zhang Z, Ma J, Mu S. Stabilizing Fe-N-C catalysts as model for oxygen reduction reaction, vol. 8; 2021, e2102209. https://doi.org/10.1002/advs.202102209.

[48] Zhang P, Chen H, Zhu H, Chen K, Li T, Zhao Y, Li J, Hu R, Huang S, Zhu W, Liu Y, Pan Y. Inter-site structural heterogeneity induction of single atom Fe catalysts for robust oxygen reduction. Nat Commun 2024;15:2062. https://doi.org/10.1038/s41467-024-46389-3.

[49] Zhu W, Pei Y, Liu Y, Zhang J, Qin Y, Yin Y, Guiver M. Mass transfer in a Co/N/C catalyst layer for the anion exchange membrane fuel cell. ACS Appl Mater Interfaces 2020;12:32842–50. https://doi.org/10.1021/acsami.0c08829.

[50] Jia C, Zhao Y, Song S, Sun Q, Meyer Q, Liu S, Shen Y, Zhao C. Highly ordered hierarchical porous single-atom Fe catalyst with promoted mass transfer for efficient electroreduction of CO_2. Adv Energy Mater 2023;13:2302007. https://doi.org/10.1002/aenm.202302007.

[51] Liu X, Xi X, Liao Y, Huang L, Liu J, Chen H, Yi Y, Long J, Zhang J, Fu X, Luo J. Deciphering the enhanced oxygen reduction reaction activity of $PrBa_{0.5}Sr_{0.5}Co_{1.5}Fe_{0.5}O_{5+\delta}$ via constructing negative thermal expansion offset for high-performance solid oxide fuel cell. Appl Catal B Environ 2024;359:124509. https://doi.org/10.1016/j.apcatb.2024.124509.

[52] Lee S, Kim J, Chung D, Yoo J, Lee H, Kim M, Mun B, Kwon S, Sung Y, Hyeon T. Design principle of Fe-N-C electrocatalysts: how to optimize multimodal porous

structures? J Am Chem Soc 2019;141:2035–45. https://doi.org/10.1021/jacs.8b11129.

[53] Li R, Zhao H, Wang L, Zhou Q, Yang X, Jiang L, Luo X, Yu J, Wei J, Mu S. Strengthened d–p orbital hybridization and hydrogen diffusion in a hollow N-doped porous carbon/Ru cluster catalyst system for hydrogen evolution reactions. Chem Sci 2025;16:4383–91. https://doi.org/10.1039/d4sc08498e.

[54] Liu ZQ, Liang X, Ma FX, Xiong YX, Zhang G, Chen G, Zhen L, Xu CY. Decoration of NiFe-LDH nanodots endows lower fe-d band center of Fe1-N-C hollow nanorods as bifunctional oxygen electrocatalysts with small overpotential gap. Adv Energy Mater 2023;13:2203609. https://doi.org/10.1002/aenm.202203609.

[55] Ma FX, Liang X, Liu ZH, Chen Y, Liu ZQ, Zhang W, Zhen L, Zeng XC, Xu CY. Impeding thermal atomization enables synthesizing Fe_2N cluster liganded single fe-atom catalyst for highly efficient oxygen reduction reaction. Angew Chem Int Ed 2025;64:e202504935. https://doi.org/10.1002/anie.202504935.

[56] Gu M, Tao L, Dastan D, Dang J, Fang T, An B. Metal-modified C_3N_1 monolayer sensors for battery instability monitoring. J Mater Chem A 2024;12:15254–64. https://doi.org/10.1039/d4ta00645c.

[57] Tao L, Dastan D, Wang W, Poldorn P, Meng X, Wu M, Zhao H, Zhang H, Li L, An B. Metal-decorated InN monolayer senses N_2 against CO_2. ACS Appl Mater Interfaces 2023;15:12534–44. https://doi.org/10.1021/acsami.2c21463.

[58] Nejadsattari F, Stadnik Z. Spin polarized density functional theory calculations of the electronic structure and magnetism of the 112 type iron pnictide compound $EuFeAs_2$. Sci Rep 2021;11:12113. https://doi.org/10.1038/s41598-021-91301-4.

[59] Franke-Lang R, Kowal J. Analysis of electrochemical impedance spectroscopy on zinc-air batteries using the distribution of relaxation times. Batteries 2021;7:56. https://doi.org/10.3390/batteries7030056.